ORIGINAL ARTICLE

A mixed-mode E-FEM approach for the study of local fracture processes in heterogeneous quasi-brittle materials

A. Ortega · E. Roubin · Y. Malecot ⬤ · L. Daudeville

Abstract This paper studies the use of the Embedded Finite Element Method (E-FEM) for the numerical modelling of triaxial fracture processes in non-homogeneous quasi-brittle materials. The E-FEM framework used in this study combines two kinematics enhancements: a weak discontinuity allowing the model to account for material heterogeneities and a strong discontinuity allowing the model to represent local fractures. The strong discontinuity features enriched fracture kinematics that allow the modelling of all typical fracture modes in three dimensions. A brief review is done of past work using similar enriched finite element frameworks to approach this problem. The work continues by establishing the theoretical basis of each kind of discontinuity formulation and their superposition through the Hu-Washizu variational principle. Three groups of numerical simulations are presented afterwards for discussing the performance of this combined E-FEM model: homogeneous sample simulations, simple heterogeneous sample simulations and simulations considering a realistic heterogeneous morphology coming from an actual concrete sample. Comparisons are made with another E-FEM model considering a single local fracture mode approach and with previous experimental data. A concluding statement is made on the benefits and challenges identified for the E-FEM framework in this kind of applications.

A. Ortega · E. Roubin · Y. Malecot (✉) · L. Daudeville
Univ. Grenoble Alpes, CNRS, Grenoble INP, 3SR,
F-38000 Grenoble, France
e-mail: yann.malecot@univ-grenoble-alpes.fr

1 Introduction

The numerical study of fracture phenomena in composite materials requires a detailed consideration of their heterogeneous structure, which contributes to the emergence of complex and unexpected mechanical behaviours. Multiscale analysis approaches have been devised in recent decades to develop mathematical models capable of capturing and predicting their response [10]. Classical approaches are based on homogenisation principles, where it is assumed that it is possible to represent a given composite material as a completely homogeneous domain whose mechanical behaviour is governed by a sufficiently complex material law taking parameters from studies at smaller scales. As an example, the representative volume element (RVE) is a widely spread approach that has been successfully used both in academic research and industry [34, 50].

Any of these homogenisation approaches require the analysis of composite materials at smaller scales

where the effects of heterogeneities can be assessed in accurate manner through their spatial layout, material properties and possible local fractures.

It is clear that any multiscale approach should have an efficient yet sufficiently accurate numerical analysis method at the smaller scales to fulfill all homogenisation requirements in a reasonable time frame. On this matter, the conventional finite element method presents considerable challenges both in the problem of heterogeneity distributions and in the explicit modeling of local fractures. On one hand, a mesh has to be adapted to represent the regions having different material phases. Depending on the natural shapes of these phases and the kind of information that can be measured about them on a 3D setting, intensive adaptive meshing techniques might be required to ensure mesh continuity through these regions while maintaining an accurate depiction of all material interfaces. This will compromise the resulting quality of the element domains. Element distortions and any other kind of geometrical anomalies will have an impact on the quality of results coming from the numerical analysis as a whole [36]. Excessive mesh density requirements to avoid bad quality issues will translate into long computational solving times.

On the other hand, the modelling of a fracture poses numerous critical challenges for a standard approach [49]. The path of the fracture should be explicitly identified and delimited *beforehand* on the mesh itself. Spontaneous failure calculations can also be implemented, but the standard methods do not possess any mathematical features capable of modelling fracture separation and/or propagation other than complete element stiffness damage mechanisms or even direct element removal under certain failure criteria. While these techniques have gained acceptance in both academy and industry for their ease of use, they are well known to produce considerable solution stability problems and modelling limitations [38, 48].

Advanced finite element approaches provide with attractive solutions to overcome the aforementioned problems on local scale material modelling, proposing integrating frameworks capable of representing both material heterogeneities and enriched local cracks using non-adaptive meshes. Among them we can find the Extended Finite Element Methods (X-FEM) [14, 44], the Base Force Element Method (B-FEM) [31, 32], the Augmented Finite Element Method (AFEM) [9] or the Embedded Finite Element Methods [18, 27, 35], among

others. Many of them are well-endowed with a mathematical flexibility capable of modelling different kinds of discontinuities to account for a variety of material phases and local fracture modes. They do this through mathematical enhancements on their supporting functions whether in a nodal base (X-FEM), through their elemental mechanical fields (E-FEM) or through new mechanical state variables (B-FEM). Some of them are even mesh-less, in the sense that their supporting functions do not depend on a definite division of elemental domains in space. The representation capability of these approaches is greatly enhanced at the expense of increasing operational and implementation complexities.

In this sense, the E-FEM framework, being the choice of the authors of this work for the current study, retains a reasonable balance between mathematical complexity and representational capability. This is mainly because it is based on the method of incompatible modes [16, 37], allowing the building of independent mechanical field enhancements on each element without ensuring rigorous global continuity. From an operational standpoint, this allows working all heterogeneity and fracture mathematical enhancements in an internal-element fashion, with the possibility to use operator-split methods [15] and thus condensing all element internal effects before attempting a global displacement solution step, whether linear or nonlinear. The E-FEM framework can then be developed in such a way that the global FEM numerical solution engine may be left untouched, enabling the support of a variety of available FEM solution platforms for implementation.

The authors of this work have chosen to focus on the use of the E-FEM framework for approaching the problem of triaxial failure in quasi-brittle materials. In Section 2, a review is made on how the E-FEM framework has recently evolved to approach this problem. In Section 3, the theoretical basis of the E-FEM framework used for this study is briefly described. It makes the integration of a weak and a generalized strong discontinuity model. No detailed development of each of the discontinuity formulations will be done as the bases have already been discussed in other works [21, 22, 29, 35, 51].

Section 4 will introduce the numerical simulations done using this generalized E-FEM approach to discuss its performance in different problem scenarios allowing to scrutinise each of its enhancements in

progressive fashion. Three different kinds of simulations will be presented in this work: homogeneous, simple heterogeneous and realistic heterogeneous. Homogeneous sample simulations will show how the strong discontinuity component of this E-FEM framework manages to capture stress triaxiality dependence in a known fracture process. Afterwards, simple heterogeneous simulations will feature a single spherical inclusion within an homogeneous matrix material considering different load conditions to discuss on the mixed 3D fracture processes unfolding due to the presence of different material phases on a simple layout. The final set of simulations feature a model of an extract of an actual concrete sample as conceived and tested under a compression load setup considering triaxial confinement. A comparison is made with respect to another typical E-FEM model considering a single fracture kinematic mode approach as well as an experimental test reference to make. Section 5 will close this work with a final word on the overall effectiveness of the E-FEM framework, with potential future works.

2 Evolution of the E-FEM framework approaching composite quasi-brittle failure problems

From the founding works that established the main base of the E-FEM framework [30, 37], this analysis approach was originally conceived to model localisation phenomena in general materials as an alternative to standard techniques with adapted meshes. It started with the idea of using weak discontinuity enhancements to represent the presence of shear localisation bands, associating specific damage behaviour laws to all domains falling between two parallel lines having an arbitrary separation (shear band thickness). As the mathematical depth of these developments evolved, the framework began to turn towards the use of strong discontinuities equipped with discrete or regularized crack behaviour laws to gain objectivity in the definition of strain localisation regions [18, 27].

Applications to quasi-brittle materials began to emerge at this stage, but only for one or two-dimensional problems [7, 12]. The pioneering work by Wells and Sluys [51] started with a full deployment of the approach for 3D problems, pushing the boundaries of the framework and evidencing new theoretical

weaknesses in the mathematical structure of strong discontinuity enhancements. They managed to implement the E-FEM framework for a linear tetrahedron including the rigid body displacement crack kinematic modes of normal separation and sliding, making the comparison between variationally symmetric and asymmetric strong discontinuity enhancements. In all these applications, the local fracture interface is defined as a plane.

At the same time, the works on improving mathematical robustness and kinematic consistency in the framework are sustained by the notable work of Jirasek and Oliver [18, 27, 28] in the early 2000s. Non-symmetrical variational schemes were favored to achieve consistent modelling of both statics and kinematics simultaneously. An enrichment of the fracture formulation was explored by implicitly incorporating a rotational degree of freedom in the kinematics of the local fracture plane of a constant stress triangle (CST) element [1], establishing the basis for enriched fracture kinematics through non-uniform strong discontinuity functions. The idea of having fully local enriched fracture modes for improving the consistency of fracture kinematics was later developed in detail on a 2D setting [22]. The authors managed to fully equip fracture kinematics with translational and rotational degrees of freedom in addition to the capability for one of the segregated domains of the element to have a simple lateral tension/compression mode. This allowed to reach new levels of variational consistency and better element internal equilibrium conditions, while having internal fracture variables that really described a physically meaningful state of the local fracture. The idea was further used in [4, 5, 8, 33, 43] and finally in the works developed in [29], where a deep theoretical assessment was made for its generalisation on a 3D setting. The present work considers this last development.

Concerning the applications to heterogeneous quasi-brittle fracture, the interest of multiscale approaches and the eventual need to incorporate the E-FEM framework into homogenisation procedures began with the notable works by Markovic [25]. In particular, it was Markovic who set the point of departure of heterogeneity modelling by reviving the effective use of the weak discontinuity formulation taking the foundations of previous works on the X-FEM approach [45]. This line of research gave rise to the first successful integration of strong and weak

discontinuities within the framework for one-dimensional bar elements in [2, 15]. In these works, an idealized 3D heterogeneity layout composed by perfectly spherical inclusions within a homogeneous matrix was used for the modelling of concrete samples. While this method was successful in predicting typical tensile resistance values for concrete, the disadvantage was that it did not return satisfactory values for tension/compression resistance ratios. The use of 1D elements also prevented having an objective perspective of local stress and strain field distributions.

This line of research began its first truly 3D solid element approach in the work done by Roubin et al. [35]. The 3D generalisation of the weak discontinuity enhancement model for heterogeneities was based on the works of Markovic [25], while a strong discontinuity model equipped with a discrete traction separation law was used for local fractures. The strong discontinuity model was capable of representing a single fracture mode of normal separation, activated by a Rankine localisation criterion and followed by an exponential traction-separation law. The representation of heterogeneity distributions was evolved to make use of probabilistic excursion sets, which enhanced the random nature of material phases improving their packaging quality and conserving a degree of smoothness on their interfaces. Despite the limitation of using a single fracture mode kinematics approach, typical tension and compression resistance ratios were found to be more reasonable than the previous works with 1D bars. Hauseux [13] later achieved the simulation of fracture sliding modes (mode II) with the same framework in the context of simulations of excavations of geomaterials, still based on a single fracture and activated by means of a Mohr-Coulomb localisation criterion. The works of Stamati [40, 41] added a new dimension to the E-FEM framework experimental validation by means of test setups having *in-situ* measurements in concrete samples that allowed direct comparisons with numerical simulations at the mesoscale.

One of the most discussed characteristics of these E-FEM models is the lack of cross-elemental continuity for the emerging cracks. As the mathematical foundations of these enhancements are intrinsically based on the method of incompatible modes [16, 37],

there is no guarantee to keep continuity of a local crack to neighboring elements once one of them starts to develop. This leads to the simultaneous creation of multiple local cracks that, by the mere mechanism of stiffness damaging and internal force redistribution, will tend to favour a *spontaneous* coalescence phenomenon giving rise to a larger scale fracture without explicitly aiming for it. While nonlocal crack continuity tracking methods within the E-FEM framework have already been well studied and implemented in multiple applications for homogeneous material simulations [5, 19, 53], the line of research currently discussed ([2, 13, 35, 41, 42]) intentionally keeps the locally discontinuous nature of the E-FEM models to favour this behaviour in the context of complex heterogeneous materials. This decision is supported by multiple studies that favour the hypothesis of multi-cracks at smaller scales contributing to the emergence of larger fracture processes in such materials [3, 26].

In other recent lines of research, the E-FEM framework has evolved to provide answers to more complex modelling problems, such as electromechanical phenomena [23], where local element fractures, already enriched with nine kinematic modes, are further enhanced with electric potential modes under a strictly local elemental condensation scheme. A successful application of the E-FEM approach to fluid mechanics is done by Idelsohn et al. [17], where once again the locality of the E-FEM framework is exploited to multi-fluid moving interface problems. Multiscale schemes integrating the E-FEM in a poromechanics setting can be founds in the recent works of Lu et al. [24] and Cusini et al. [6]. Local crack reclosure and healing models have been also explored through single (3D) [46] and multiple (2D) [11] local kinematic fracture mode schemes. The performance of the E-FEM framework approaching dynamic crack propagation problems is assessed in the works of [52]. The works of Kakarla [20] explore the possibility to model multiple crossing cracks within a single element, allowing to consider a more complex evolution of the internal load direction.

The current work will continue in this line with a generalized strong discontinuity model integrated with a weak discontinuity model for considering the presence of material heterogeneities.

3 Double enhancement E-FEM formulation with generalized fracture kinematic modes

The fundamental modelling of an embedded discontinuity within a finite element starts by having a body representing an elemental domain Ω_e having boundaries $\partial\Omega$. The body is crossed by a surface Γ_d that establishes the presence of a strain (weak) or displacement (strong) discontinuity, partitioning the complete domain in two subregions Ω^+ and Ω^-. The subregion interface Γ_d is characterized at each of its points by normal and parallel unit vectors $\hat{\boldsymbol{n}}$, $\hat{\boldsymbol{t}}$ and $\hat{\boldsymbol{m}}$, respectively. These are commonly referred to as the *local frame* on the E-FEM context. A typical scheme in two dimensions can be appreciated in Figure 1.

From now on, while all theoretical premises presented in this study are applicable to a wide variety of finite element geometries and configurations, this study will mostly particularise all works to a specific base 3D finite element: a linear tetrahedron. The interface Γ_d representing whether the local element rupture or the division between different material phases is assumed to be planar, characterized by a constant and unique local frame ($\hat{\boldsymbol{n}}$, $\hat{\boldsymbol{t}}$, $\hat{\boldsymbol{m}}$) and segmenting a given tetrahedron in two subvolumes V^- and V^+.

3.1 Weak discontinuity formulation

The weak discontinuity formulation within the E-FEM framework is used to model the presence of different material phases within a single element domain. It introduces a jump on the strain field to account for the presence of different materials while still retaining displacement continuity (thus the reason of calling it *weak* discontinuity). Its basic construction assumes that a general displacement field $\boldsymbol{u}$ can be decomposed as the sum of a homogeneous standard displacement $\overline{\boldsymbol{u}}$ and an enhanced displacement field $\widetilde{\boldsymbol{u}}$ in the following general form:
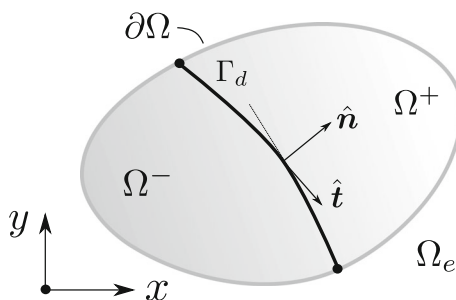
$$\boldsymbol{u} = \overline{\boldsymbol{u}} + \widetilde{\boldsymbol{u}} \tag{1}$$

where the enhancement $\widetilde{\boldsymbol{u}}$ has the role of adding a displacement slope discontinuity representing the change in material characteristics, *i.e.*, the jump on the strain field. A typical particularisation to a tetrahedron element can be appreciated in Figure 2(a), assigning different linear elastic material properties $E^\pm$, $v^\pm$ to each of the subdomains $\Omega^\pm$.

The model taken for all developments and simulations presented in this study is the one typically used on the line of research followed in [35] and analysed in detailed in [21]:

Weak discontinuity enhancement

$$\widetilde{\boldsymbol{u}} = \Theta\hat{\boldsymbol{n}} \cdot (\boldsymbol{x} - \boldsymbol{x}_{\Gamma_d})\big([\varepsilon]_n\hat{\boldsymbol{n}} + [\varepsilon]_t\hat{\boldsymbol{t}} + [\varepsilon]_m\hat{\boldsymbol{m}}\big) \tag{2}$$

$$\Theta = \begin{cases} \Theta^+ = \dfrac{V^-}{V} & x \in \Omega^+ \\[2mm] \Theta^- = -\dfrac{V^+}{V} & x \in \Omega^- \end{cases} \tag{3}$$

where $\hat{\boldsymbol{n}} \cdot (\boldsymbol{x} - \boldsymbol{x}_{\Gamma_d})$ is the normal distance from a given point $\boldsymbol{x}$ to the nearest location $\boldsymbol{x}_{\Gamma_d}$ of the surface Γ_d. The internal variables $[\varepsilon]_n$, $[\varepsilon]_t$, $[\varepsilon]_m$ characterise the magnitude of the strain jump when crossing Γ_d.

3.2 Strong discontinuity formulation

The role of the strong discontinuity in this work is to model the displacement jump associated to an element local fracture. It is defined by having a general displacement field $\boldsymbol{u}$ expressed as a continuous base field $\overline{\boldsymbol{u}}$ added to a Heaviside function $\mathcal{H}_{\Gamma_d}$, whose trigger location is that of the discontinuity surface Γ_d. It is described as:

$$\boldsymbol{u} = \overline{\boldsymbol{u}} + \mathcal{H}_{\Gamma_d}[|\boldsymbol{u}|], \tag{4}$$

where $[|\boldsymbol{u}|]$ is a vector that describes the displacement jump in each direction, This study takes advantage of a non-uniform definition of $[|\boldsymbol{u}|]$ field components at the interface to represent fully enriched fracture kinematics describing the motion of the Ω^+ domain with respect to Ω^-. In general, rigid body translations

Fig. 1 Basic schematic of an embedded discontinuity (whether weak or strong) in 2D

Fig. 2 Schematic of the weak and strong discontinuities for tetrahedral element. (Color figure online)

(a) Weak discontinuity.

(b) Strong discontinuity.
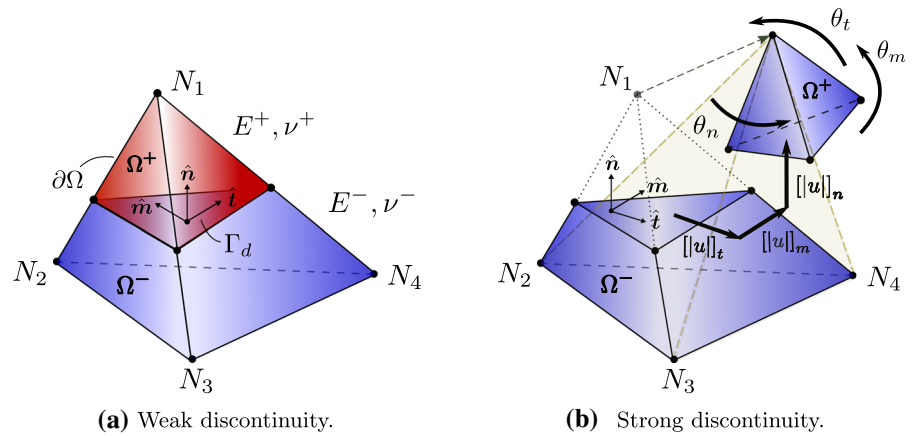
$[|u|]_n, [|u|]_t, [|u|]_m$, rigid body rotations $\theta_n, \theta_t, \theta_m$ and simple tensile-compressive strains in each direction $\epsilon_n, \epsilon_t, \epsilon_m$ can be all identified on a general linear definition for each component of $[|u|]$. Figure 2(b) illustrates an example of this enriched set of fracture kinematic modes for a domain Ω^+ on a tetrahedron. The centroid of Γ_d is taken as the origin for defining all rigid body modes.

Eq. 4 does not allow a coherent imposition of boundary conditions, since those that are prescribed on Ω^- pertain the vector $\overline{u}$, while the remaining that belong to Ω^+ have their information contained in $\overline{u} + \mathcal{H}_{\Gamma_d}[|u|]$. To overcome this, a typical technique in the framework [27] has been to introduce a new auxiliary field φ function allowing for the following change of variables:

$$\hat{u} = \overline{u} + \varphi[|u|], \qquad (5)$$

where $\hat{u}$ is a unified vector that has its node displacements completely consistent with u while retaining the strong discontinuity information *continuously spread* inside thanks to the φ function. The only mathematical constraint φ is required to satisfy is the following:

$$\varphi = \begin{cases} 1 & x_i \in \Omega^+ \\ 0 & x_i \in \Omega^- \end{cases} \quad i = 1, 2, 3, 4 \qquad (6)$$

where x_i denotes a nodal position.

A more robust definition of φ is made in this work to avoid variational and kinematic inconsistencies as much as possible ([29, 51]). In this work, it will feature a cubic, piece-wise (Ω^+, Ω^- domains), individual definition per each local direction ($\hat{n}, \hat{t}, \hat{m}$) of $[|u|]$.

Designating local coordinates as (ξ, η, ζ), a compound φ can be expressed using a complete cubic polynomial base P_3:

$$\varphi = \begin{bmatrix} \varphi_n^{\pm} & 0 & 0 \\ 0 & \varphi_t^{\pm} & 0 \\ 0 & 0 & \varphi_m^{\pm} \end{bmatrix}$$

$$\varphi_j^{\pm} = P_3^T \alpha_j^{\pm} \qquad j = n, t, m$$

$$P_3 = \begin{bmatrix} 1 & \xi & \eta & \zeta & \xi\eta & \eta\zeta & \xi\zeta & \xi^2 & \eta^2 & \zeta^2 \\ \xi^2\eta & \xi\eta^2 & \eta^2\zeta & \eta\zeta^2 & \xi^2\zeta & \xi\zeta^2 & \xi\eta\zeta & \xi^3 & \eta^3 & \zeta^3 \end{bmatrix}^T$$

$$\alpha = \begin{bmatrix} \alpha_n^+ & \alpha_n^- & \alpha_t^+ & \alpha_t^- & \alpha_m^+ & \alpha_m^- \end{bmatrix}^T$$

$$\qquad (7)$$

This extended definition for φ allows the usage of $\alpha_j^{\pm}$ coefficients as free parameters to aid the satisfaction of numerous consistency constraints that are helpful on building a solid strong discontinuity formulation structure [29].

Introducing this variable change along with the generalised definition for fracture kinematics through a kinematic modes vector ξ allows reaching an enriched definition for the displacement field accounting for a strong discontinuity:

Strong discontinuity enhancement

$$u = \hat{u} + (\mathcal{H}_\Gamma - \varphi)\mathbf{J}\xi \qquad (8)$$

where $\mathbf{J}$ is an interpolation matrix based on local ξ, η, ζ coordinates operating on ξ. The latter contains all the unknown fracture kinematic modes of translation, rotation and simple strain:

$$\mathbf{J} = \begin{bmatrix} 1 & 0 & 0 & 0 & \zeta & -\eta & \xi & 0 & 0 \\ 0 & 1 & 0 & -\zeta & 0 & \xi & 0 & \eta & 0 \\ 0 & 0 & 1 & \eta & -\xi & 0 & 0 & 0 & \zeta \end{bmatrix}$$

(9a)

$$\boldsymbol{\xi}^T = \begin{bmatrix} [|u|]_{n_0} & [|u|]_{t_0} & [|u|]_{m_0} & \theta_n & \theta_t & \theta_m & \epsilon_{nn} & \epsilon_{tt} & \epsilon_{mm} \end{bmatrix}^T$$

(9b)

3.3 Variational integration of both discontinuity enhancements

To model both heterogeneities and local element fractures in the same element domain, the aforementioned definitions have to be integrated within a unique mathematical framework. The main assumption by doing this superposition is that both the material interface and the fracture interface coincide perfectly at the same surface during all the analysis. Based on the previous definitions, the following can be reached by making a linear superposition:

$$\boldsymbol{u} = \hat{\boldsymbol{u}} + \tilde{\boldsymbol{u}} + (\mathcal{H}_\Gamma - \varphi)\mathbf{J}\boldsymbol{\xi}$$

(10)

The Hu-Washizu framework has been chosen as the variational principle in this work. It treats displacement, strain and stress fields (*real fields*) $(\boldsymbol{u}, \boldsymbol{\varepsilon}, \boldsymbol{\sigma})$ as well as their respective variations (*virtual fields*) $(\delta\boldsymbol{u}, \delta\boldsymbol{\varepsilon}, \delta\boldsymbol{\sigma})$ as completely independent of each other. This allows a considerable flexibility on the discretisation strategy for each of the fields. Expressed already in a Voigt vector format, the equation system entailed by this variational framework is the following one:

$$\int_\Omega \partial\delta\boldsymbol{u}^t\boldsymbol{\sigma}\,dV - \int_\Omega \delta\boldsymbol{u}^t\boldsymbol{f}_b\,dV - \int_{\partial\Omega} \delta\boldsymbol{u}^t\boldsymbol{t}\,dA = 0$$

(11a)

$$\int_{\Omega_e} \delta\boldsymbol{\sigma}^t(\partial\boldsymbol{u} - \boldsymbol{\varepsilon})dV = 0$$

(11b)

$$\int_{\Omega_e} \delta\boldsymbol{\varepsilon}^t(\boldsymbol{\sigma}(\boldsymbol{\varepsilon}) - \boldsymbol{\sigma})dV = 0$$

(11c)

where $\boldsymbol{t}$ and $\boldsymbol{f}_b$ are the boundary traction and body force vectors. The ∂ operator is the equivalent of the symmetric gradient operator ∇^s (defined as $\nabla^s(\bullet) = \frac{1}{2}[\nabla(\bullet)^T + \nabla(\bullet)]$) in a Voigt format. An

important distinction is made between the stress field $\boldsymbol{\sigma}(\boldsymbol{\varepsilon})$ that is calculated from a linear elastic constitutive law taking the real strain field $\boldsymbol{\varepsilon}$ and the real stress field $\boldsymbol{\sigma}$, which is independent. In the same way, the real strain field $\boldsymbol{\varepsilon}$ is not necessarily equal to the symmetric gradient of the displacement field $\partial\boldsymbol{u}$.

The discretisation strategy for each of the real (**and** virtual) fields must be able to capture the physics sought by the study allowing at the same time for mathematical simplicity and numerical efficiency. This work will keep with the strategy already presented for both strong and weak discontinuity enhancements presented in [21, 29]. A summary of the mathematical works on the variational framework is also presented therein. The choice of a linear tetrahedron as the base element allows for the use of a *full integration scheme*.

Among the most important resulting expressions from the entire variational analysis, we can find an equation governing the internal-external force balance:

$$\boldsymbol{f}_{int}^e = \int_\Omega \mathbf{B}^t\boldsymbol{\sigma}(\boldsymbol{\varepsilon})\,dV = \boldsymbol{f}_{ext}^e$$

(12a)

$$\boldsymbol{f}_{int}^e = \mathbf{K}_{bb}\boldsymbol{d} + \mathbf{K}_{bw}[|\boldsymbol{\varepsilon}|] + \mathbf{K}_{bs}\boldsymbol{\xi}$$

(12b)

where $\mathbf{B}$ is the standard operator corresponding to the derivatives of the shape functions of the base element and $\mathbf{K}_{bb}, \mathbf{K}_{bw}, \mathbf{K}_{bs}$ are resulting stiffness matrix operators corresponding to weak and strong discontinuity internal variables $[|\boldsymbol{\varepsilon}|], \boldsymbol{\xi}$, as well as the standard nodal displacement vector $\boldsymbol{d}$. There will be also another equation governing the local weak discontinuity behavior:

$$\mathbf{K}_{wb}\boldsymbol{d} + \mathbf{K}_{ww}[|\boldsymbol{\varepsilon}|] + \mathbf{K}_{ws}\boldsymbol{\xi} = 0$$

(13)

where, again, $\mathbf{K}_{wb}, \mathbf{K}_{ww}, \mathbf{K}_{ws}$ are resulting stiffness matrix operators corresponding to all main local and global variables in the model. And, finally, an expression dictating local strong discontinuity behavior, which relates the cohesive traction vector $\boldsymbol{T}$ associated to a local fracture plane and the bulk stresses on the elemental domains $(\boldsymbol{\sigma}^+, \boldsymbol{\sigma}^-)$. The weak discontinuity variable $[|\boldsymbol{\varepsilon}|]$ can be reduced by means of Eq. 13 to reach an expression which is function only of the standard nodal displacements vector $\boldsymbol{d}$ and the fracture kinematic modes vector $\boldsymbol{\xi}$:

$$T = \frac{1}{V}\left(V^+ \boldsymbol{\sigma}^+ + V^- \boldsymbol{\sigma}^-\right) \tag{14a}$$

$$T = \mathbf{K}_{s^*b}\boldsymbol{d} + \mathbf{K}_{s^*w}[|\boldsymbol{\varepsilon}|] + \mathbf{K}_{s^*s}\boldsymbol{\xi} \tag{14b}$$

$$T = \boldsymbol{T}_e + \mathbf{M}\boldsymbol{\xi} \tag{14c}$$

$$\boldsymbol{T}_e = \mathbf{K}_e\boldsymbol{d} \tag{14d}$$

where, again, $\mathbf{K}_{s^*b}, \mathbf{K}_{s^*w}, \mathbf{K}_{s^*s}$ are the corresponding stiffness matrix operators in this governing equation. Eq. 14c is the standard form for presenting the traction vector associated with the local crack on the current E-FEM framework. Eq. 14c determines the state of crack traction depending on loads and the kinematic state of the crack. On one hand, the $\boldsymbol{T}_e$ vector represents the traction imposed by the **current load** in the element, depending on the standard displacement vector $\boldsymbol{d}$. It is a *variable mechanical demand* that will guide the evolution of the fracture process within the element. The $\mathbf{M}$ matrix, referred to in this work as the *fracture stiffness*, accounts for the mechanical impact of having a kinematic state of fracture. It does not depend on load but only on a mixture between element geometry characteristics and basic properties of the surface Γ_d. This composition of load effects and the crack state yield a current state for $\boldsymbol{T}$. In turn, $\boldsymbol{T}$ is to be *controlled* (damaged) by a discrete traction separation law.

From now on, the description of all remaining mathematical structures in the model will be done on the local frame $\hat{\boldsymbol{n}}, \hat{\boldsymbol{t}}, \hat{\boldsymbol{m}}$ (with the respective ξ, η, ζ coordinates). For instance, the traction vector $\boldsymbol{T}$ is now expressed as $\boldsymbol{T} = \begin{bmatrix} T_n & T_t & T_m \end{bmatrix}^T$.

3.4 Localisation criteria

A localisation criterion is required to designate a local failure within an element and to start introducing the impact of fracture mechanics through the expressions developed earlier plus a set of traction separation laws (Section 3.5).

Localisation also has the secondary role in the case of homogeneous elements of determining the orientation and location of the fracture surface Γ_d. The base element explored in this work remains a linear tetrahedron whose real stress field has been set as uniform. Thus, a localisation criterion can objectively determine the orientation but not the exact location of the local fracture. On this matter, the authors of this study have decided to take the approach followed in [13, 35] and make Γ_d to pass through the centroid of the element reaching localisation. For all heterogeneous elements, it has been already stated that the crack plane will be made perfectly coincident with the material interface plane.

This work has taken the traction vector components T_n, T_t, T_m to articulate the localisation criterion on the normal-shear stress space (σ_n, τ) on Γ_d. A completely closed criterion has been built by composing a piecewise function with three different sub-criteria:

- A **Rankine** criterion, represented by a straight vertical line on the (σ_n, τ) plane with a *positive* abscissa σ_{y_R}. For a homogeneous element, this criterion sets the orientation of the local crack plane as the plane of the maximum principal stress σ_1.
- A **compression** limit criterion. This is also represented by a straight vertical line on the (σ_n, τ) plane with a *negative* abscissa σ_{y_C}. For a homogeneous element, this criterion sets the orientation of the local crack plane as the plane of the minimum principal stress (maximum compression) σ_3.
- A **Mohr-Coulomb** criterion, represented by a couple of symmetric lines (with respect to the σ_n axis) described with the equation $\tau = \pm C \mp (\tan\psi)\sigma_n$. For a homogeneous element, this criterion sets the orientation of the local crack plane as the one maximising the combined shear stress dictated by the Mohr-Coulomb criterion.

This piece-wise curve remains very simple (4 material parameters) and ensures that all possible stress failure states are covered. Figure 3 illustrates this compound criterion. The element is considered in a localised state if a load trajectory on the (σ_n, τ) plane intersects the compound criterion, establishing an intersection point (σ_y, τ_y) that serves as the initial *yield* parameters for operating the respective traction-separation laws (Section 3.5).

The collection of traction-separation laws also involve the crack surface stress components **not explicitly included** in the traction vector $\boldsymbol{T}$, as it is just a projection of the entire state of stresses $\boldsymbol{\sigma}$ on the $\hat{\boldsymbol{n}}$ direction. An estimation of the initial yield values $\sigma_{y_{tt}}, \sigma_{y_{tm}}, \sigma_{y_{mm}}$ for these components $\sigma_{tt}, \sigma_{tm}, \sigma_{mm}$ is done base on the evolution of the entire state of stresses at the interface just before the localisation event.

Fig. 3 The envelope localisation criterion on the (σ_n, τ) plane used in this work showing notable intersecting points. A proportional load is shown beginning on a zero state up to reaching an intersection with the curve at (σ_y, τ_y)
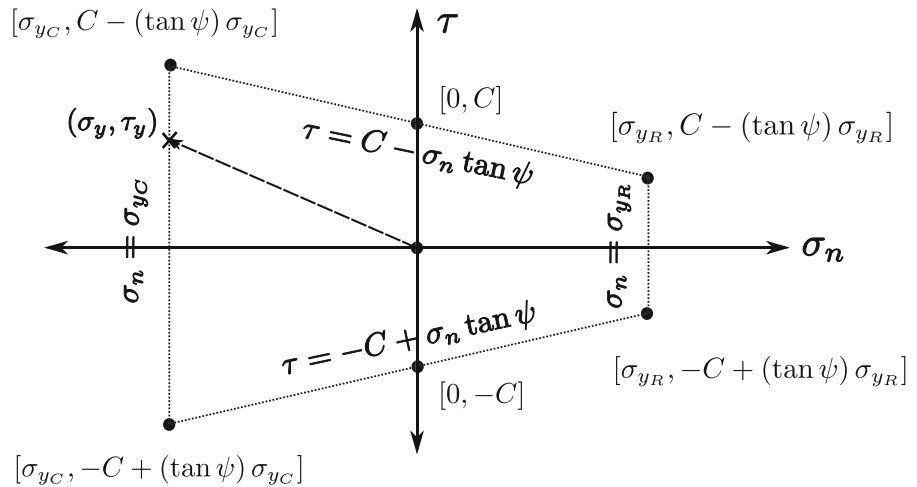
3.5 Traction-separation laws and local fracture mechanics

After having reached a state of localization, a local state of rupture is established in the element, and the behavior is governed by a traction-separation law. It describes the evolution of the components of the traction vector $\boldsymbol{T}$ at the local interface of fracture according to the kinematic fracture variables. Since the enriched generalized kinematics proposed for the local fracture possesses 9 different modes, 9 relations are required to fully determine the complete internal state of an element.

A first set of three traction-separation is proposed to ensure the process of damage to the main components T_n, T_m, T_t of the cohesive traction vector:

$$\boldsymbol{T} = \boldsymbol{T}_e + \mathbf{M}\boldsymbol{\xi} = \boldsymbol{q} \tag{15a}$$

$$T_n = T_{e_n} + \sum_{k}^{9} M_{n_k}\xi_k = q_n \tag{15b}$$

$$T_t = T_{e_t} + \sum_{k}^{9} M_{t_k}\xi_k = q_t \tag{15c}$$

$$T_m = T_{e_m} + \sum_{k}^{9} M_{m_k}\xi_k = q_m \tag{15d}$$

where q_j $(j = n, t, m)$ are damage functions that will control the evolution of each of the traction components. k goes through each of the fracture kinematic modes. To simplify the approach, it was decided not to

involve all nine kinematic modes in the q_j functions. The emphasis will be on the kinematic rigid body modes $[[u]]_{n_0}, [[u]]_{t_0}, [[u]]_{m_0}$ to control the evolution of the damage process for all traction vector components. The vector $\boldsymbol{q}$ is then defined using exponential functions as:

$$\boldsymbol{q} = \begin{bmatrix} q_n \\ q_t \\ q_m \end{bmatrix} = \begin{bmatrix} \sigma_{y_n} \\ \sigma_{y_t} \\ \sigma_{y_m} \end{bmatrix} e^{-\left(\frac{\sigma_{y_n}}{G_{fI}}[[u]]_{n_0} + \frac{\sigma_{y_t}}{G_{fII}}[[u]]_{t_0} + \frac{\sigma_{y_m}}{G_{fII}}[[u]]_{m_0} \right)} \tag{16}$$

where $\sigma_{y_n}, \sigma_{y_t}, \sigma_{y_m}$ are the initial resistance values defined from the localisation calculations. The constants G_{fI} and G_{fII} are defined as physical internal failure parameters which can be perceived as fracture surface energies for mode I and mode II failures coming from the classical theory of fracture mechanics, respectively.

This set of equations is further enriched with a more detailed local fracture mechanics capable of representing crack reclosure phenomena, sliding by friction based on the amplitude of normal contact forces and the possibility of additional microporosity compaction. The definition of these local physics is based entirely on the rigid kinematic failure modes linked to the translation of a rigid body $[[u]]_{n_0}, [[u]]_{t_0}, [[u]]_{m_0}$. Figure 4 shows respectively the behavior proposed for the kinematic modes of normal separation and of parallel sliding. Cumulative normal separation and sliding displacements $|u|_n, |u|_t, |u|_m$ are defined to keep track of the current damaged state of the local crack and to
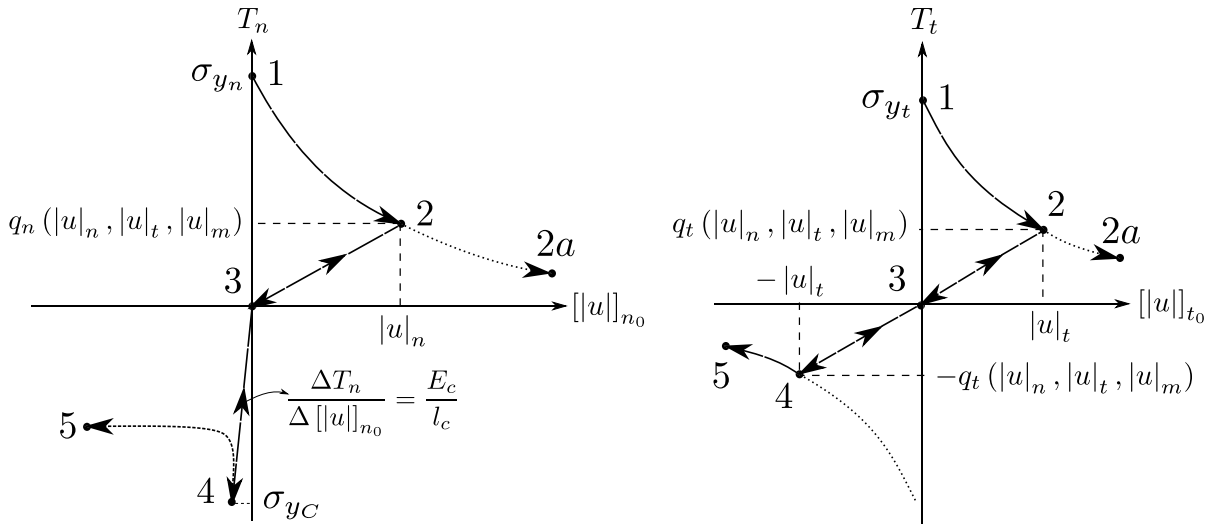
Fig. 4 Illustration for reversible and irreversible behaviours for crack normal separation (left) and sliding kinematic modes (right). The path from 1 to 2 is irreversible, while 2-3 is depicted as a reversible path forced by an insufficient load that fails to continue crack evolution to point 2a. If the load is reversed enough, the crack can will be eventually closed (3). Further load reversibility induces compression for the left plot and sliding on the opposite side of the crack for the right plot (3-4). Eventually, one can even reach irreversible behaviour zones once again (4-5)

define the thresholds that determine further damage or a crack reclosure state. The reclosure (or sliding reversal) behaviors have been defined as simple linear functions from the previously accumulated damage states $(q_j)_{i-1}$ down to zero. In the case of a complete crack normal reclosure, normal forces start to develop if further compression is registered. The associated stiffness is defined as the young modulus of the softer material E_c between both $\pm$ domains normalized by the element characteristic length l_c. If the local crack is compressed enough so that it reaches the compaction limit σ_{y_c}, the interface will irreversibly drop its mechanical resistance down to a terminal value. For the model used in the final simulations presented later in this work, this terminal value has been set to zero.

With these considerations, the set of principal traction separation laws finally becomes:

$$T_{e_n} + M_{nn}[[u]]_{n_0} = \begin{cases} q_n & [[u]]_{n_0}|u|_n \\ \dfrac{(q_n)_{i-1}}{|u|_n}[[u]]_{n_0} & 0 \leq [[u]]_{n_0} \leq |u|_n \\ \dfrac{E_c}{l_c}[[u]]_{n_0} & \sigma_{y_c} \leq T_n \leq 0 \\ q_C & T_n \leq \sigma_{y_c} \end{cases}$$

(17a)

$$T_{e_t} + M_{tt}[[u]]_{t_0} \pm T_{\mu_t} = \begin{cases} q_t^\pm & \left|[[u]]_{t_0}\right||u|_t \\ \dfrac{(q_t)_{i-1}}{|u|_t}[[u]]_{t_0} & \left|[[u]]_{t_0}\right||u|_t \end{cases}$$

(17b)

$$T_{e_m} + M_{mm}[[u]]_{m_0} \pm T_{\mu_m} = \begin{cases} q_m^\pm\left|[[u]]_{m_0}\right||u|_m \\ \dfrac{(q_m)_{i-1}}{|u|_m}[[u]]_{m_0}\left|[[u]]_{m_0}\right||u|_m \end{cases}$$

(17c)

A second set of three traction-separation equations is proposed to damage the out-of-plane stress components $\sigma_{tt}, \sigma_{tm}, \sigma_{mm}$:

$$T'_{e_t} + \sum_k^9 M'_{t_k}\xi_k = q_{tt} \tag{18a}$$

$$T'_{e_m} + \sum_k^9 M'_{m_k}\xi_k = q_{tm} \tag{18b}$$

$$T''_{e_m} + \sum_k^9 M''_{m_k}\xi_k = q_{mm} \tag{18c}$$

where alternate stiffness matrices $\mathbf{M}'$ and $\mathbf{M}''$ are derived considering projections of the entire crack

stress state onto the $\hat{t}$ and $\hat{m}$ directions, respectively. Also:

$$
\begin{bmatrix} q_{tt} \\ q_{tm} \\ q_{mm} \end{bmatrix} = \begin{bmatrix} \sigma_{y_{tt}} \\ \sigma_{y_{tm}} \\ \sigma_{y_{mm}} \end{bmatrix} e^{-\left(\frac{\sigma_{yn}}{G_{fI}}[|u|]_{n_0} + \frac{\sigma_{yt}}{G_{fII}}[|u|]_{t_0} + \frac{\sigma_{ym}}{G_{fII}}[|u|]_{m_0}\right)}
$$

(19)

where $\sigma_{y_{tt}}, \sigma_{y_{tm}}, \sigma_{y_{mm}}$ are again retrieved from the localisation calculations.

In the end, a set of three closing equations is proposed to complete the system. These equations do not have a strictly physical meaning, and only serve to reinforce the hypothesis that the modes of rupture by translation of the rigid body $[|u|]_{n_0}, [|u|]_{t_0}, [|u|]_{m_0}$ are the most predominant for determine the local fracture mechanics. These equations make it possible to weakly decouple the first of these kinematic modes from the other equations of the system:

$$
\sum_{k=4}^{9} M_{n_k} \xi_k = 0 \tag{20a}
$$

$$
\sum_{k=4}^{9} M_{t_k} \xi_k = 0 \tag{20b}
$$

$$
\sum_{k=4}^{9} M_{m_k} \xi_k = 0 \tag{20c}
$$

3.6 Linearisation of the model and global solution

The linearisation process for the application of non-linear global iterative solutions can be accomplished by departing from the main relations governing each of the internal discontinuity variables $[|\varepsilon|]$, ξ and the nodal displacements d (Eqs. 13, 12b and the system 17a-20c).

The first and most standard case is the global internal-external force balance, in which the dependent nonlinear variable increment is taken as the global residual of internal and external nodal forces from successive iterations k and $k+1$ for a set of assembled element force balance equations. For this, the linearisation of Eq. 12b is assembled repeatedly ($\mathbb{A}$ operator) for all n_e elements currently iterating during the application of a load step $p+1$ coming from an already solved step p. This yields the following:

$$
\overset{n_{el}}{\underset{}{\mathbb{A}}} \left\{ \mathbf{K}_{bb}\Delta d \Big|_{p+1}^{(k+1)} + \mathbf{K}_{bw}\Delta[|\varepsilon|] \Big|_{p+1}^{(k+1)} + \mathbf{K}_{bs}\Delta\boldsymbol{\xi} \Big|_{p+1}^{(k+1)} \right\}
$$
$$
= -\overset{n_{el}}{\underset{}{\mathbb{A}}} \left\{ \boldsymbol{f}_{int}^e \Big|_{p+1}^{(k+1)} - \boldsymbol{f}_{ext}^e \Big|_{p} \right\}
$$

(21)

In the E-FEM framework, which is based on the principle of incompatible modes [37], no global continuity is guaranteed for any of the internal variables characterising both weak and strong discontinuities. Hence, none of the linearisations associated to Eqs. 13, 17a-20c go through any conventional assembly process. Indeed, there will be one relation to be satisfied for each element in an independent fashion. For instance, the weak discontinuity governing relation (Eq. 13) can also be linearised by defining its balance through a dependent variable $\boldsymbol{\Phi}_w$ at element level, which is always sought as zero during the nonlinear solution process. Taking increments in this expression leads to the following:

$$
\mathbf{K}_{wb}\Delta d \Big|_{p+1}^{(k+1)} + \mathbf{K}_{ww}\Delta[|\varepsilon|] \Big|_{p+1}^{(k+1)} + \mathbf{K}_{ws}\Delta\xi \Big|_{p+1}^{(k+1)} = \Delta\Phi_w \Big|_{p+1}
$$
$$
= \mathbf{0} - \Phi_w \Big|_{p+1}^{k}
$$

(22)

where Eq. 22 is never assembled in a global format.

Linearisation of the strong discontinuity model governing relations is not evident since different sets of traction separation laws were incorporated with different considerations (Eqs. 17a- 17c, 18a-18c) and there are also the closing relations coming from purely algebraic considerations (Eqs. 20a-20a). Once the nine relations have been linearised, they can be *assembled* to build a single matrix block-based equation to pack down the nine relations into a single linearised expression defining $\Delta\boldsymbol{\Phi}_0$ as a collective dependent increment:

$$
\overline{\mathbf{K}_{s^*b}}\Delta d \Big|_{p+1}^{(k+1)} + \overline{\mathbf{K}_{s^*w}}\Delta[|\varepsilon|] \Big|_{p+1}^{(k+1)} + \overline{\mathbf{K}_{s^*s}}\Delta\xi \Big|_{p+1}^{(k+1)}
$$
$$
= \Delta\Phi_0 = \mathbf{0} - \Phi_0 \Big|_{p+1}^{k}
$$

(23)

where the matrices $\overline{\mathbf{K}_{s^*b}}$, $\overline{\mathbf{K}_{s^*w}}$, $\overline{\mathbf{K}_{s^*s}}$ contain the aforementioned small-scale assembly of linearisations of all traction separation laws and closing equations previously developed.

Having all these linearisations, the same global solution approach in [35] is followed. A complete linearised system is first built in a block-matrix format as:

$$\begin{bmatrix} \mathbf{K}_{bb} & \mathbf{K}_{bw} & \mathbf{K}_{bs} \\ \mathbf{K}_{wb} & \mathbf{K}_{ww} & \mathbf{K}_{ws} \\ \overline{\mathbf{K}_{s^*b}} & \overline{\mathbf{K}_{s^*w}} & \overline{\mathbf{K}_{s^*s}} \end{bmatrix}_{p+1}^{(k)} \begin{bmatrix} \Delta \boldsymbol{d} \\ \Delta [|\boldsymbol{\varepsilon}|] \\ \Delta \boldsymbol{\xi} \end{bmatrix}_{p+1}^{(k)} = \begin{bmatrix} -\overset{n_{el}}{\mathbb{A}} \{ \boldsymbol{f}_{int}^e - \boldsymbol{f}_{ext}^e \} \\ -\boldsymbol{\Phi}_w \\ -\boldsymbol{\Phi}_0 \end{bmatrix}_{p+1}^{(k)}$$

(24)

Considering, once again, that the weak and strong discontinuity models only have immediate influence at a local level, the typical global strategy solution for a nonlinear iteration $k+1$ is to take the solution of the standard displacement vector $\boldsymbol{d}$ solved on the previous iteration k to internally update the *actual state* of the weak and strong discontinuity variables $[|\boldsymbol{\varepsilon}|], \boldsymbol{\xi}$ using the nonlinear equation system (Eqs. 17a-20c) and Eq. 13. With this, the linear system 24 is condensed in the $\Delta[|\boldsymbol{\varepsilon}|], \Delta \boldsymbol{\xi}$ increments to reach a final expression involving exclusively the increment of the standard nodal vector $\Delta \boldsymbol{d}$ and a condensed *elemental* stiffness matrix $\mathbf{K}_{sc}$, which is to one to be assembled and eventually used to execute a numerical method of choice by a standard finite element global solution engine. The final condensed global FEM equilibrium equation system has the following form:

$$\overset{n_{el}}{\mathbb{A}} \left\{ \mathbf{K}_{sc} \Big|_{p+1}^{(k+1)} \Delta \boldsymbol{d} \Big|_{p+1}^{(k+1)} \right\} = -\overset{n_{el}}{\mathbb{A}} \{ \boldsymbol{f}_{int}^e - \boldsymbol{f}_{ext}^e \} \Big|_{p+1}^{(k)}$$

(25a)

$$\mathbf{K}_{sc} \Big|_{p+1}^{(k+1)} = \mathbf{K}_{bb} - \begin{bmatrix} \mathbf{K}_{bw} & \mathbf{K}_{bs} \end{bmatrix} \begin{bmatrix} \mathbf{K}_{ww} & \mathbf{K}_{ws} \\ \overline{\mathbf{K}_{s^*w}} & \overline{\mathbf{K}_{s^*s}} \end{bmatrix}^{-1} \begin{bmatrix} \mathbf{K}_{wb} \\ \overline{\mathbf{K}_{s^*b}} \end{bmatrix} \Big|_{p+1}^{(k)}$$

(25b)

The calculation of the residuals at each nonlinear iteration can be calculated as:

$$\boldsymbol{f}_{int}^e \Big|_{p+1}^{(k)} = V_e \mathbf{B}^t \boldsymbol{\sigma} \Big|_{p+1}^{(k)} = \mathbf{K}_{bb} \boldsymbol{d} + \mathbf{K}_{bw} [|\boldsymbol{\varepsilon}|] + \mathbf{K}_{bs} \boldsymbol{\xi} \Big|_{p+1}^{(k)}$$

(26)

4 Numerical Simulations

In this section, an implementation done within the FEAP program [47] will be tested under a variety of conditions to study the response of the generalised E-FEM formulation and its capability for predicting different kinds of fracture processes. The simulations will be done side-by-side with a previous numerical

model having a single kinematic mode E-FEM framework [13, 35, 40].

Three types of simulations will be presented to the reader:

- **Homogeneous sample simulations**. These setups will feature completely homogeneous elements without the presence of any weak discontinuities. Torsional load simulations will take place to discuss the emergence of *controlled* tridimensional fracture processes. By *controlled*, the authors of this work imply that a specific pattern for a tridimensional fracture process is already expected for a given simulation setup knowing its geometry and load conditions.
- **Basic heterogeneous sample simulations**. A cubical homogeneous matrix material domain having a spherical inclusion in the center is prescribed with a compressive load. This allows to test the weak discontinuity and its influence on the initiation and growth of fractures in this model, tracking the development of the local crack networks.
- **Micro-concrete sample simulations**. Cubical samples are modelled containing realistic heterogeneity distributions coming from actual micro-concrete samples used during the test campaigns for the research done by Stamati [41]. With the associated experimental data of this research, a correlation for the Mode II parameters used in the proposed E-FEM formulation of this work is performed. Having this, the detailed study of the intricate evolution of the local crack networks, their eventual coalescence and the entire tridimensional fracture processes emerging in the model is studied.

4.1 Homogeneous simulations

The proposed numerical model for the following simulations is a cubic domain having a torsion load on its upper face and fixing its lower face completely. The length L_c of the cube is 10 mm, and it features a non-structured tetrahedral mesh having a characteristic length of 0.1 mm. The torsional load has been exerted by means of a displacement profile. A maximum torsion angle of $0.03°$ was prescribed to be model

(equivalent to a sample shear strain of 3.7×10^{-4} mm/mm at the outermost fibers).

A special feature of this setup is that it is has a *weakened material band* with a height Δh at the center of the model. Here, the first occurrence of crack initiation is promoted by letting the remaining material (above and below the band) to have slightly increased strength values. This region has exactly the same linear material parameters as the remaining model. This is done to avoid any spurious concentrations near the vicinity of the regions having boundary conditions. For these simulations, the middle band has been set to $\Delta h = 0.8 L_c$.

Material properties for both E-FEM formulations (single mode [13, 35, 40] and generalised modes [29]) can be found in Table 1. The generalised modes formulation takes all the parameters in the table, while the previous formulation (single mode) only takes the linear and those related to Mode I local failures. For top and bottom thin layers of material, the only difference is the increased σ_{y_R}, C parameters (by 10%) as previously discussed, applicable for both formulation cases.

It is of interest to study how the fracture process switches its nature during the global post-localisation stage. Differences are expected within the single mode and generalised mode formulations when shear and fracture sliding demands become more significant during the load application. To make a clear point on this, Figures 5 and 6 are proposed to illustrate the initiation and consolidation of the local crack networks for both models.

Figure 5 focuses on the initiation of the fracture process, fixed at the first load step where the global behaviour of the model becomes nonlinear. Here, it can be observed how both models start to promote the emergence of classical 45° fracture processes for a brittle or quasi-brittle material under torsion, forming an angular periodic pattern of local crack networks. Each of the cube model faces presents this initiation as

these are the outermost surface layers of the body under torsion. The entirety of these local crack networks feature elements that have localised under the mode I criterion, *i.e.*, all in tensile failure (shown as blue elements within the transparent cube).

Figure 6 captures the final state of both numerical simulations at the end of torsion application. At this stage, the fracture process related to mode I failure and kinematics has already completely developed in both models, having the four local crack networks converging in a slightly helical fashion at the core of the cubical sample. From this point, a critical divergence in behaviour can be acknowledged between both formulations. The single mode formulation is not able to predict any significant further evolution of the fracture process, and the generalised formulation allows a complete change of nature for it: it starts to focus exclusively on mode II failure and kinematics (red elements). This allows to finalise the entire fracture process.

This difference can be better appreciated in Figure 7, where a global reaction response of the model was monitored with respect to load application in both models. The vertical reaction was chosen since it was the simplest to measure and still provides information about the current energy being stored in all the material domain. Indeed, a clear divergence in global post-localisation behaviour can be easily spotted, where the single mode curve goes off to increase without any perceptible bound, while the generalised modes curve suggests a clear loss of mechanical resistance in the model.

4.2 Basic Heterogeneous Simulations

The next set of simulations aims to study the effect of weak discontinuities in the formation and propagation of a tridimensional fracture process considering a simple heterogeneity distribution and having simple

Table 1 Input material parameters used for the E-FEM formulations in the homogeneous torsion simulations

E-FEM input parameters, homogeneous torsion			
Linear	$E = 14000$ MPa	$v = 0.2$	
Mode I	$\sigma_{y_R} = 9$ MPa	$G_{f_I} = 0.00001$ MPa·mm	
Mode II	$C = 36$ MPa	$\tan \phi = 0.6$	$G_{f_{II}} = 0.6$ MPa·mm $\mu_m = 0.6$
Compaction	$\sigma_{y_C} = -500$ MPa		

$$\beta_1 = 0.012°$$

Single mode   Generalised modes
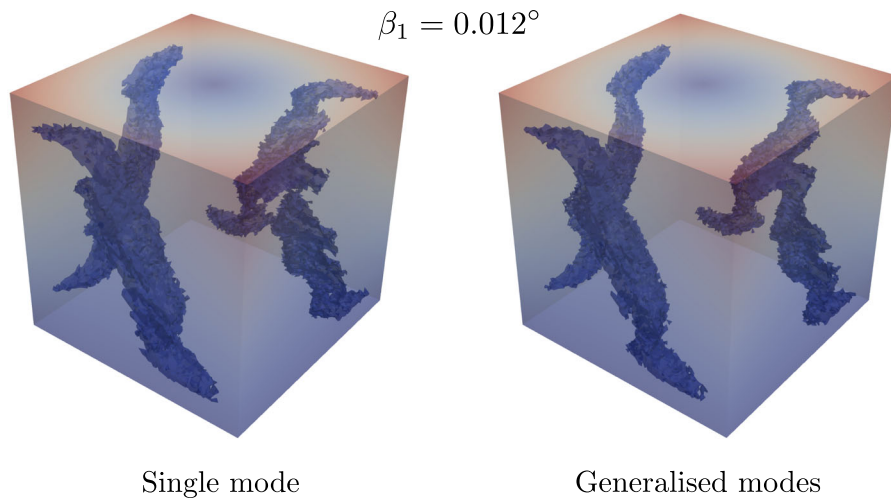
Fig. 5 Elements conforming the local crack networks within the cube domain for a torsion load just right after beginning global nonlinear behaviour. All blue elements correspond to a

tensile (mode I) localisations. The cube shows also a translucent contour of resultant nodal displacements having red as maximums and blue as minimums. (Color figure online)

$$\beta_2 = 0.03°$$

Single mode   Generalised modes
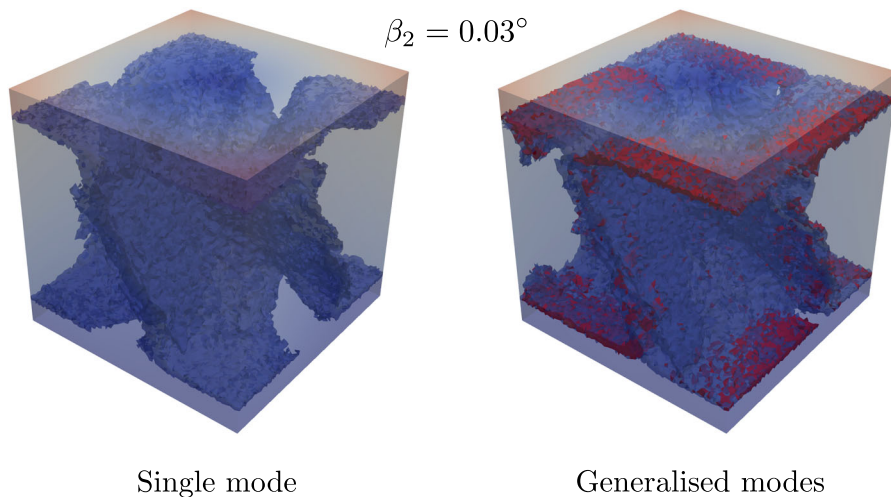
Fig. 6 Elements conforming the local crack networks within the cube domain for a torsion load at the end of load application. All blue elements correspond to a tensile (mode I) localisations, and red elements are associated to a mode II localisations. The

fracture process has not significantly evolved for the single mode formulation, whereas the generalised model predicts a mode II behaviour for the conclusion of the fracture process. (Color figure online)

load cases. The main simulation setup will focus on a homogeneous matrix domain having the presence of a spherical inclusion made of a stronger material. Fracture processes are expected to start at the material interfaces and to evolve in particular ways depending on each load case.

The geometry of the heterogeneous sample is a cube with a side dimension of 10 mm having a perfectly spherical inclusion of 6 mm of diameter.

This material phase distribution is projected onto a mesh conformed by regular (good aspect ratios) but unstructured tetrahedral elements. The average characteristic length of the elements is 0.15 mm. As a consequence, a number of these elements have been *cut* by the inclusion boundaries, generating a number of material interfaces modelled through the weak discontinuity approach. Figure 8 shows the general mesh built and already projected with the material
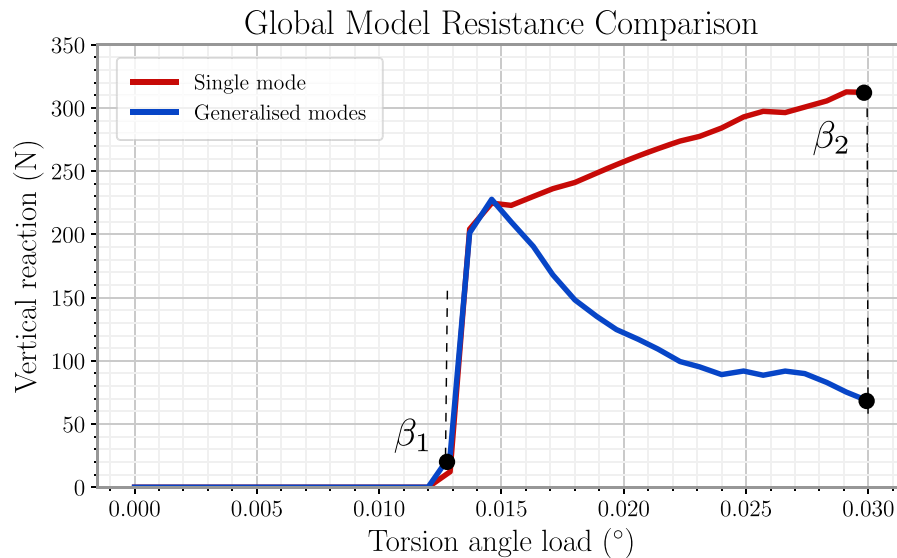
Fig. 7 Total vertical reaction measured with both models during the entire simulation. (Color figure online)

phases for all these simulations, as well as the generated weak discontinuity interfaces for the sphere boundary.

The parameters given for both single and generalised modes E-FEM formulations can be found in Table 2. These resemble those coming from typical mortar and aggregate material properties found in a concrete mixture. Note that the interface failure parameters take the resistance limits coming from the weakest material phase (mortar).

Linear and mode I properties found in Table 2 were taken from the calibration process made in the works of Stamati [40], which are used for both single mode formulations [35] and generalised modes formulations [29]. All remaining parameters have been set based on a correlation with experimental results from an actual concrete sample.

A pure compressive load case has been contemplated for the current simulations. The load is exerted until a full tridimensional fracture process is developed in the entire domain, reaching a terminal point in which the cohesion between the mortar and the inclusion can be considered as *completely broken*, rendering the model no longer capable of offering any kind of mechanical resistance.

There is a significant difference in both global resistance and ductility (defined hereby as the sample strain corresponding to maximum resistance ε_{max}) between single mode and generalised modes formulations. Thus, different maximum compression distances have to be used to fully develop their respective fracture processes: -0.05 mm and -0.1 mm, respectively. Figure 9 shows the behaviour of globally defined stress-strain curves for both models.

Each step as identified with a strain value relative to the sample ductility (ε_{max}), covering states before and during the maximum resistance load steps as well as complete global post-localisation behaviours. Figure 10 shows a three step description ($\varepsilon_1 - \varepsilon_3$) for the case of the single mode formulation, displaying only blue element networks corresponding to mode I local failures.

The single mode formulation presents a double band initiation at the lower and upper hemispheres of the inclusion for then propagating completely around it (ε_1). At maximum resistance, the fracture process begins to extend out of the sphere vicinity in a rather uncontrolled and irregular fashion (ε_2). At post-localisation, the single mode formulation exhibits a sudden fall in resistance, and the fracture process seems to evolve in an arbitrary manner (ε_3). Cohesion between the inclusion and matrix material is completely broken, finishing ending the evolution of the fracture process.

Figure 11 describe again three evolution steps ($\varepsilon_1 - \varepsilon_3$) for the case of the generalised modes formulation. A two band network initiation and an eventual takeover of the inclusion surface is also observed for this formulation. The behaviour starts to
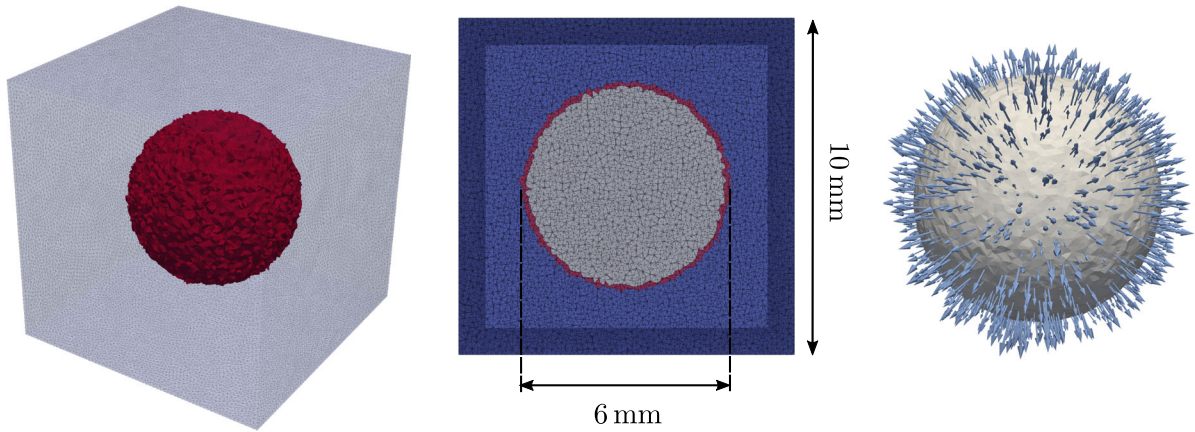
Fig. 8 General model mesh description for the basic heterogeneous setups featuring a single spherical inclusion. On the left, the mesh of all elements *touched* by the inclusion sphere within a translucent mesh of the remaining bulk of the material matrix domain. In the middle, a mid-cut section of the entire mesh, distinguishing exclusive mortar material elements (in blue), exclusive aggregate material elements (in gray) and bi-phase elements (in red) generally found at the sphere border. On the right, a sphere reconstructed by taking the resulting planar interface surfaces Γ_d coming from each bi-phase element, along with their respective normal vector. (Color figure online)

Table 2 Input material parameters used for the E-FEM formulations in the simple heterogeneous simulations in this work

E-FEM input parameters, simple heterogeneous compression				
Mortar-only elements				
Linear	$E = 14000$ MPa	$v = 0.2$		
Mode I	$\sigma_{y_R} = 9$ MPa	$G_{f_I} = 0.0001$ MPa·mm		
Mode II	$C = 36$ MPa	$\tan\phi = 0.6$	$G_{f_{II}} = 0.6$ MPa·mm	$\mu_m = 0.6$
Compaction	$\sigma_{yc} = -500$ MPa			
Aggregate-only elements				
Linear	$E = 70000$ MPa	$v = 0.2$		
Mode I	$\sigma_{y_R} = 45$ MPa	$G_{f_I} = 0.0001$ MPa·mm		
Mode II	$C = 180$ MPa	$\tan\phi = 0.6$	$G_{f_{II}} = 0.6$ MPa·mm	$\mu_m = 0.6$
Compaction	$\sigma_{yc} = -500$ MPa			
Interface elements (- for mortar, + for aggregate)				
Linear	$E^+ = 70000$ MPa	$v^+ = 0.2$	$E^- = 14000$ MPa	$v^- = 0.2$
Mode I	$\sigma_{y_R} = 9$ MPa	$G_{f_I} = 0.0001$ MPa·mm		
Mode II	$C = 36$ MPa	$\tan\phi = 0.6$	$G_{f_{II}} = 0.6$ MPa·mm	$\mu_m = 0.6$
Compaction	$\sigma_{yc} = -500$ MPa			

diverge from this point, where shear-compression zones initiate at the top and bottom faces of the mortar domain. These regions contain exclusively elements associated to a mode II local failure, and also in a crack closure state, presenting frictional behaviour. These zones extend vertically until fusing with the inclusion surface fracture process (ε_1). At maximum resistance, a middle shear band emerges and surrounds the inclusion surface completely (ε_2), and finally the fracture extends from this band to all the mortar domain in a vertical fashion, finishing the tridimensional fracture process (ε_3). These results suggest that this predominant mode II state serves to provide more ductility and resistance to the sample.

Overall, it is observed once again that both formulations share certain stages of the behaviour of the tridimensional fracture process, but the generalised model is able to grant a larger insight of further steps where mode II local failures and compression having frictional sliding become significantly important.

Fig. 9 Global stress-strain curves under a compressive load for the single spherical inclusion setups for both single mode and generalised modes formulations. (Color figure online)
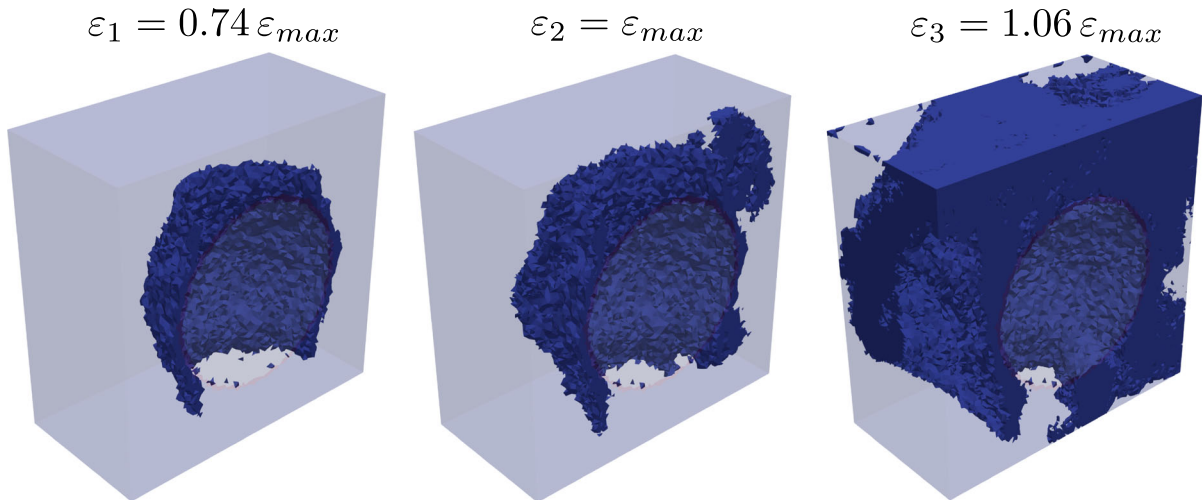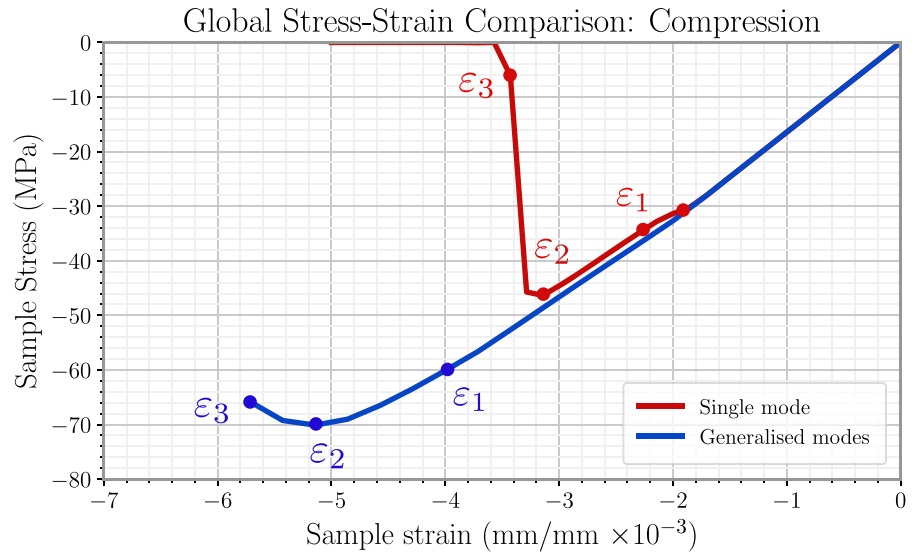
Fig. 10 Fracture process evolution for the compressive load case considering the single mode formulation. Three different stages are reported at different strains relative to the maximum resistance strain ε_{max}. (Color figure online)

4.3 Realistic concrete sample simulations

The last section in this work pertains the numerical simulations of samples having a realistic material heterogeneity (pores, aggregates and mortar). As mentioned during the introduction of this chapter, it was through the works of Stamati et al. [40–42], both through the experimental campaigns involving *in-situ* X-ray tomography measurements and the contributions to the dedicated software SPAM [39], that it was possible to process sample raw digital data to end up

with a projected mesh with all pertinent details in the coming simulation setups.

The original samples as tested in [41] have a cylindrical geometry having an average length of 20 mm and an average diameter of 10 mm. For the simulations in the present work, only a cubical subregion has been extracted from one specific micro-concrete cylindrical sample. The cube has a length dimension of $\sqrt{50} \approx 7.071$ mm. The characteristic length of the unstructured tetrahedral mesh to which the heterogeneities are projected is 0.1 mm.

$$\varepsilon_1 = 0.784\,\varepsilon_{max} \qquad \varepsilon_2 = \varepsilon_{max} \qquad \varepsilon_3 = 1.12\,\varepsilon_{max}$$
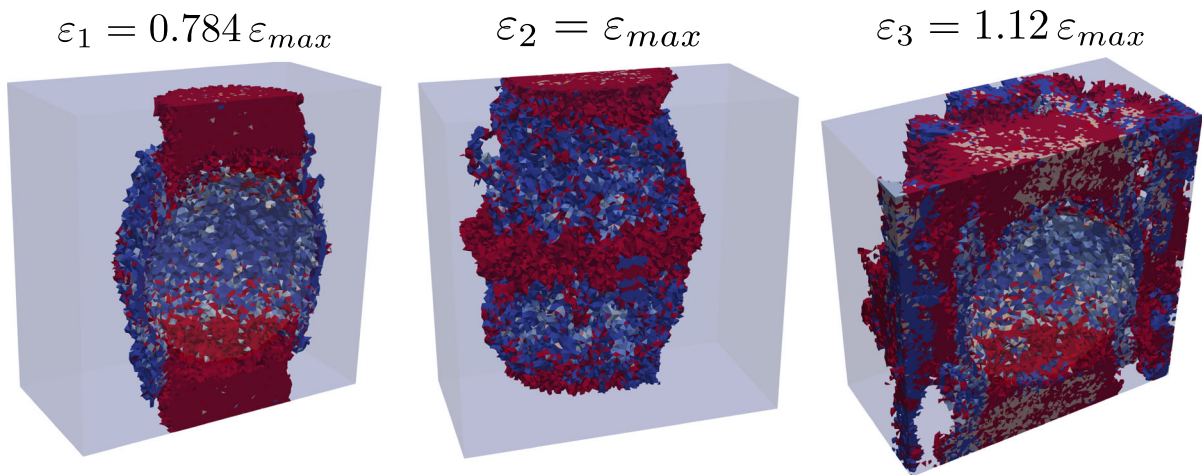
Fig. 11 Fracture process evolution for the compressive load case considering the generalised modes formulation. Colours having a blue palette denote element localisations related to mode I local failures, while the red palette corresponds to those related to mode II. The reddest colour specifically indicates elements under crack closure compression. (Color figure online)

Figure 12 shows the resulting projected mesh for the sample managed for all the following numerical simulations.

Note that the internal pore regions have been accounted for in this setup as free stress condition regions (voids).

The load cases considered for this model will be tension and compression under different levels of triaxial pre-confinement considering 0, 5, 10 and 15 MPa. This is the entire test program achieved so far by the works of Stamati et al. [42] for the mesoscale studies on this micro-concrete material. In this sense, it is important to note that the single mode I formulation [35, 40] has already gone through a calibration process using tension load experimental data, for then testing its response for all other load type cases. The general conclusions drawn by Stamati et al. [40–42] from this process can be summarised as follows:

- The single mode calibration with the tension load test data allowed to capture global nonlinear resistance behaviour (stress-strain) and local crack network distributions.
- This calibrated single model formulation, as it is, was tested to model another sample undergoing pure compression with no triaxial pre-confinement. A reasonable match concerning global resistance response was obtained (only one case with an error of 25% was identified).

- The comparisons with the results coming from the samples undergoing triaxial preconfinement reveal that the single mode formulation gradually loses prediction capability. Overall, initial global resistance predictions still remain within a reasonable margin with more deviation as confinement pressure growths (10-30% errors). Ductility (perceived as the global strain value at which maximum resistance is obtained) is not captured accurately in **any** of the preconfined cases (errors up to 50%).

Based on these findings, the authors of this work went on for correlating the additional parameters granted by the newly proposed E-FEM formulation based on the data coming from the triaxial test campaign done by Stamati [42], especially some of those concerning mode II local failures $(C, G_{f,I}, \mu)$. After multiple iterations with the generalised modes formulation, a set of parameters was found to increase overall the quality of the model prediction with respect to test results. This final set of parameters has been already presented when discussing the spherical inclusion simulations in Section 4.2. The reader can quickly refer to Table 2 to recall the specific numerical values.

From a simulation setup standpoint, triaxial confinement was implemented in two different phases: pre-confinement phase and uniaxial loading case. In the preconfinement case, a hydrostatic pressure is imposed in two of the horizontal faces of the cube
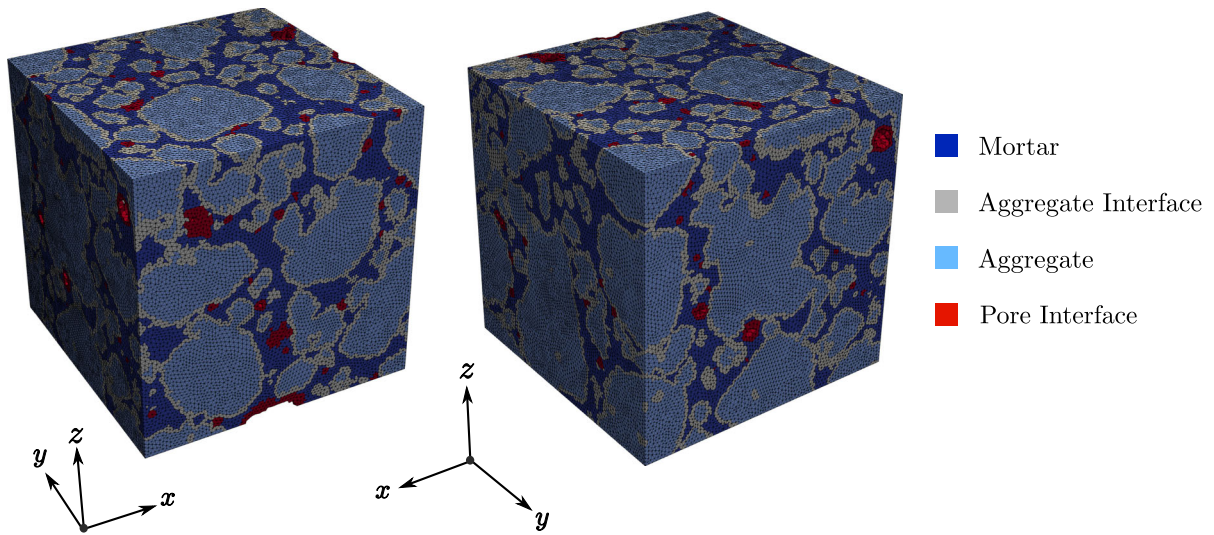
Fig. 12 Two views of the cubical mesh domain having the realistic concrete sample heterogeneity already projected. Based in this projection, element classification is shown on the right.

Pure *pore* elements were simply removed from the model to represent stress-free conditions in these regions. (Color figure online)

model (x and y), while a displacement is imposed on the upper vertical face. The amount of vertical displacement to prescribe corresponds to that granting a force reaction equalizing the pressure from the horizontal faces, thus obtaining an approximately hydrostatic state. The reason why the upper vertical face remains displacement-controlled is that it remains the face in which further uniaxial load will be specified. The remaining faces have normal displacement constraints as to avoid rigid body motion as in the models managed in previous sections. Afterwards, the uniaxial loading case just continues to increase the compressive displacement on the vertical face while maintaining the same level of lateral pressure. This is done until fully developing a fracture process in the sample.

The behaviour from the single mode I formulation, along with the reference coming from test results and the response of the generalised E-FEM model are shown in Figure 13. X markers have been placed at the maximum resistance positions for each curve, so that the reader can easily compare the corresponding ductility characteristics for the models. Results suggest that the proposed E-FEM model is able to drive the predictions closer to the test reference, in both ductility and resistance. The model tends to overshoot over the projected experimental values for low confinement pressures, eventually falling behind for 10

and 15 MPa. It should be noted that the behaviour **after** localisation cannot be assessed for any of the test data sets as the load cell was not capable of providing with reliable measurements in this phase of the test [42]. For all cases, the proposed E-FEM model exhibits a more ductile post-localisation behaviour than the single mode formulation. On the other hand, the ductility of the generalised model appears to decrease as the confinement pressure is increased, struggling each time more to keep up with the ductility imposed by the projected results.

As in the previous sections, a comparison is made by capturing the state of the local networks at different values of global strain with respect to the strain of maximum resistance ε_{max}. Figures 14 and 15 show the comparison between both models for three states approximately at the same level of global strain related to ε_{max}: one at maximum resistance, and one in global post-localisation behaviour. This is done for the case of a preconfinement pressure of 5 MPa.

Given the large amount of stress concentrators irregularly distributed in this domain, there is a large number of elements that will go through a localisation state, but not necessarily with *full participation* on the emerging tridimensional fracture process. The elements were thus filtered by considering whether the amount of crack normal separation ($[|u|]_{n_0}$) or sliding ($[|u|]_{t_0}$, $[|u|]_{m_0}$), where a general threshold of 0.4 μm

Fig. 13 Global stress-strain behaviours for both single and generalised models for tension and all compression load cases, along with the projected tendencies for the experimental results in this model. The markers identify the positions at maximum resistances for each model, which allow to compare the ductility characteristics. (Color figure online)

$$\varepsilon_2 = \varepsilon_{max}$$

Single mode   Generalised modes
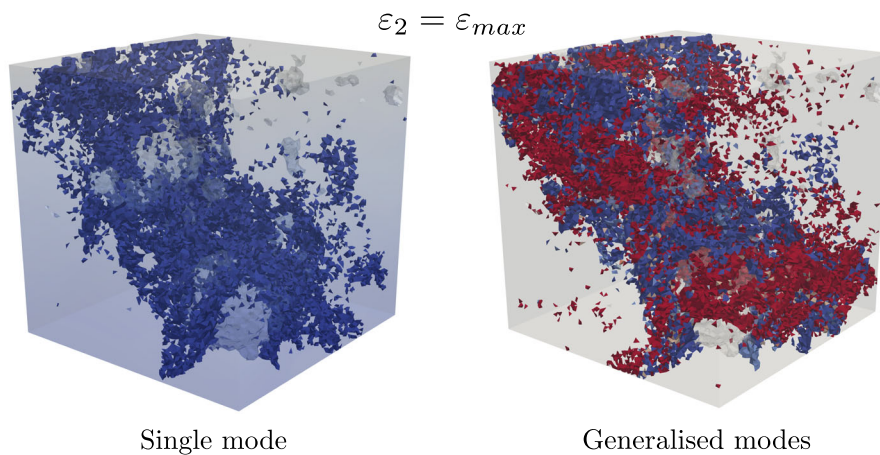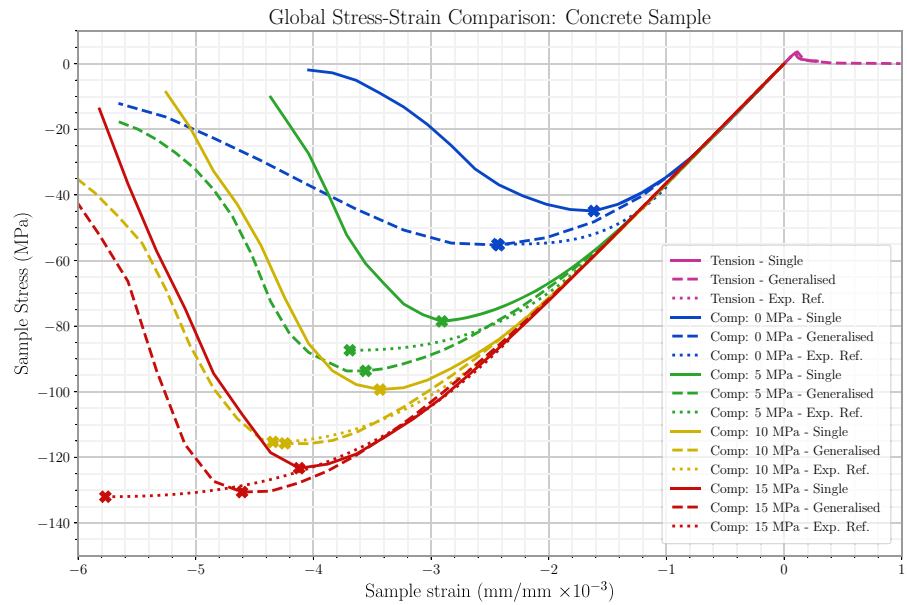
Fig. 14 State of local crack networks for the single and generalised modes in the realistic concrete sample domain numerical simulation at the state of maximum resistance, considering a confinement pressure of 5 MPa. All elements in a blue palette belong to mode I local failures, while the red palette belongs to mode II-related events. (Color figure online)

has been considered. If the elements undergo closure and local compression, a threshold of -0.2 μm of compression distance has been taken as the minimum to start displaying in figures 14 and 15.

At maximum resistance (Figure 14), a full fracture process has taken a classical 45° definite shape, and it clearly covers all the cube length scale. The participation of mode II local failures is significant for the generalised modes formulation, and almost all these elements remain in a closure/frictional state. There is already a very noticeable difference concerning global

resistances between both formulations both E-FEM formulations at this point (Figure 13). In the post-localisation stage (Figure 15), the extent of the defined global fracture remains stable, but recruiting more surrounding elements and beginning the collapse of the sample. For the generalised E-FEM formulation, it is relevant to note the emergence of elements failing under pure compaction criteria (purple colour). Results at this at the 10, 15 MPa confinement pressures suggest that the modelling behaviour for these compacted micro-regions play an important role for

$$\varepsilon_3 = 1.1\varepsilon_{max}$$

Single mode   Generalised modes
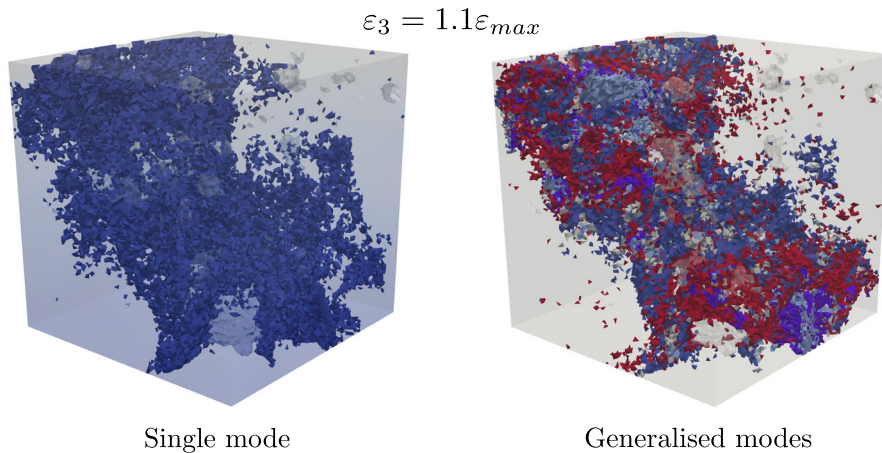
Fig. 15 State of local crack networks for the single and generalised modes in the realistic concrete sample domain numerical simulation a bit after the state of maximum resistance, considering a confinement pressure of 5 MPa. All elements in a blue palette belong to mode I local failures, while the red palette belongs to mode II-related events. Purple elements have failed under a pure compression criterion (failure by compaction). (Color figure online)

ductility at higher confinement pressures at the post-localisation stage of the concrete samples.

While the mixed-modes formulation still respects the strictly local approach desired for the E-FEM framework to grant flexibility and portability for the elemental routines, the introduction of a new set of nonlinear effects inevitably implies more complexity in the phase of numerical implementation as well as computational costs. As a reference, the numerical solution of a single case of the aforementioned realistic cubical model takes roughly 1.5 days while using the mode-I formulation while the mixed-modes formulation takes 3.3 days.

5 Conclusions

This work has introduced the reader to an integration of a generalised strong discontinuity model with a weak discontinuity model to conform a numerical analysis approach capable of delivering meaningful representations of tridimensional fracture processes for quasi-brittle materials. A theoretical background is provided, describing the fundamental mathematical aspects of the generalised fracture mode kinematics for the strong discontinuity and the weak discontinuity. A clear description of localisation criteria has been provided, along with the traction separation equation system that benefits from the generalised structure of the fracture kinematic modes to incorporate more robust local crack physics. It is worth remembering that the authors of this work gave priority to the influence of crack rigid body displacements modes (separation and sliding) for the damage-regulating definitions.

A number of numerical simulations have been done to attest to general capabilities of the generalised models for different situations. In particular, the authors find a remarkable participation of mode II mechanics on the emergence of different global and local crack network behaviours. Results suggest that a model capable of considering local sliding, compression and frictional mechanics will be able to gain more insight at the fracture processes under highly compressive or shear demands at larger scales, specifically those featuring larger ductility and resistance through more energy dissipation mechanisms.

The present work has shown that it is still possible to remain with an E-FEM framework having a *strictly local* mathematical structure, benefiting of enough simplicity without having to make a significant incursion on a global FE numerical solution platform. It should be reminded that the essence of this line of research was to achieve a sufficiently predictive advanced FE numerical model keeping its computational burdens and implementation complexities to a minimum. In this sense, the authors of this work believe that the E-FEM framework is still an attractive option worth exploring, offering unique advantages over other advanced FE techniques.

References

1. Alfaiate J, Simone A, Sluys L (2003) Non-homogeneous displacement jumps in strong embedded discontinuities. Int J Solids Struct 40:5799–5817. https://doi.org/10.1016/S0020-7683(03)00372-X

2. Benkemoun N, Hautefeuille M, Colliat JB, Ibrahimbegovic A (2010) Failure of heterogeneous materials: 3d meso scale fe models with embedded discontinuities. Int J Numer Method Eng 82:1671–1688. https://doi.org/10.1002/nme.2816

3. Chateau C, Nguyen TTT, Bornert M, Yvonnet J (2018) DVC-based image subtraction to detect microcracking in lightweight concrete. Strain 54:e12276. https://doi.org/10.1111/str.12276

4. Contrafatto L, Cuomo M, Tommaso G, Venti, D (2013) Computational issues in the finite element with embedded discontinuity method based on non-homogenous displacement jump. 10.13140/2.1.2466.4320. pp 17–20

5. Dias-da-Costa D, Alfaiate J, Sluys L, Areias P, Júlio E (2013) An embedded formulation with conforming finite elements to capture strong discontinuities. Int J Numer Methods Eng 93:224–244. https://doi.org/10.1002/nme.4393

6. Cusini M, White JA, Castelletto N, Settgast RR (2021) Simulation of coupled multiphase flow and geomechanics in porous media with embedded discrete fractures. Int J Numer Analyt Method Geomech 45:563–584. https://doi.org/10.1002/nag.3168

7. Dominguez N, Brancherie DM, Davenne L, Ibrahimbegović A (2005) Prediction of crack pattern distribution in reinforced concrete by coupling a strong discontinuity model of concrete cracking and a bond-slip of reinforcement model. Eng Comput 22:558–582

8. Dujc J, Brank B, Ibrahimbegovic A, Brancherie D (2010) An embedded crack model for failure analysis of concrete solids. Comput Concr. 7: 331

9. Essongue S, Couégnat G, Martin E (2021) Finite element modelling of traction-free cracks: Benchmarking the augmented finite element method (afem). Eng Fract Mech 253:107873. https://doi.org/10.1016/j.engfracmech.2021.107873

10. Fish J, Shek K (2000) Multiscale analysis of composite materials and structures. Compos Sci Technol 60:2547–2556. https://doi.org/10.1016/S0266-3538(00)00048-8

11. Freeman BL, Bonilla-Villalba P, Mihai IC, Alnaas WF, Jefferson AD (2020) A specialised finite element for simulating self-healing quasi-brittle materials. Adv Model Simulat Eng Sci. https://doi.org/10.1186/s40323-020-00171-4

12. Gálvez J, Planas J, Sancho J, Reyes E, Cendón D, Casati M (2013) An embedded cohesive crack model for finite element analysis of quasi-brittle materials. Eng Fract Mech 109:369–386. https://doi.org/10.1016/j.engfracmech.2012.08.021

13. Hauseux P, Roubin E, Colliat JB (2017) The embedded finite element method (e-fem) for multicracking of quasi-brittle materials. In: Shojaei AK, Shao J (eds) Porous Rock Fracture Mechanics. Woodhead Publishing, Sawston, pp 177–196

14. Huang J, Chen M, Sun J (2014) Mesoscopic characterization and modeling of microcracking in cementitious materials by the extended finite element method. Theoret Appl Mech Lett 4:041001. https://doi.org/10.1063/2.1404101

15. Ibrahimbegovic A, Melnyk S (2007) Embedded discontinuity finite element method for modeling of localized failure in heterogeneous materials with structured mesh: An alternative to extended finite element method. Computat Mech 40:149–155. https://doi.org/10.1007/s00466-006-0091-4

16. Ibrahimbegovic A, Wilson EL (1991) A modified method of incompatible modes. Commun Appl Numer Methods 7:187–194. https://doi.org/10.1002/cnm.1630070303

17. Idelsohn SR, Gimenez JM, Nigro NM (2018) Multifluid flows with weak and strong discontinuous interfaces using an elemental enriched space. Int J Numer Methods Fluids 86:750–769. https://doi.org/10.1002/fld.4477

18. Jirásek M (2000) Comparative study on finite elements with embedded cracks. Comput Methods Appl Mech Eng 188:307–330. https://doi.org/10.1016/S0045-7825(99)00154-1

19. Jirásek M, Zimmermann T (2001) Embedded crack model. part ii: combination with smeared cracks. Int J Numer Methods Eng 50:1291–1305. https://doi.org/10.1002/1097-0207(20010228)50:6⟨1291::AID-NME123.0.CO;2-Q

20. Kakarla SSHS (2020) From anisotropic damage to multiple cracks by coupling a microplane model and a strong discontinuity formulation in the Embedded Finite Element Method. Ph.D. thesis Université Paris Saclay - ENS Paris Saclay. https://tel.archives-ouvertes.fr/tel-03197956

21. Laborin AO, Roubin E, Malecot Y, Daudeville L (2021) An analysis of embedded weak discontinuity approaches for the finite element modelling of heterogeneous materials. Subm Int J Numer Methods Eng. https://doi.org/10.31224/osf.io/4cmdk

22. Linder C, Armero F (2007) Finite elements with embedded strong discontinuities for the modeling of failure in solids. Int J Numer Methods Eng 72:1391–1433. https://doi.org/10.1002/nme.2042

23. Linder C, Zhang X (2014) Three-dimensional finite elements with embedded strong discontinuities to model failure in electromechanical coupled materials. Comput Methods Appl Mech Eng 273:143–160. https://doi.org/10.1016/j.cma.2014.01.021

24. Lu M, Zhang H, Zheng Y, Zhang L (2017) A multiscale finite element method for the localization analysis of homogeneous and heterogeneous saturated porous media with embedded strong discontinuity model. Int J Numer Methods Eng 112:1439–1472. https://doi.org/10.1002/nme.5564

25. Markovic D, Niekamp R, Ibrahimbegovic A, Matthies H, Taylor R (2005) Multi-scale modeling of heterogeneous structures with inelastic constitutive behaviour: Part i - physical and mathematical aspects. Eng Comput Int J Comput Aided Eng 22:664–683. https://doi.org/10.1108/02644400510603050

26. Nguyen TT, Yvonnet J, Bornert M, Chateau C (2016) Initiation and propagation of complex 3d networks of cracks in heterogeneous quasi-brittle materials: Direct comparison between in situ testing- microct experiments and phase field

simulations. J Mech Phys Solids. https://doi.org/10.1016/j.jmps.2016.06.004

27. Oliver J (1996) Modelling strong discontinuities in solid mechanics via strain softening constitutive equations. part 1: fundamentals. Int J Numer Methods Eng. 39:3575–3600. https://doi.org/10.1002/(SICI)1097-0207(19961115)39:213575:AID-NME653.0.CO;2-E

28. Oliver J (1996) Modelling strong discontinuities in solid mechanics via strain softening constitutive equations. part 2: numerical simulation. Int J Numer Methods Eng. 39:3601–3623. https://doi.org/10.1002/(SICI)1097-0207(19961115)39:213575:AID-NME653.0.CO;2-E

29. Ortega Laborin A, Roubin E, Malecot Y, Daudeville L (2021) General consistency of strong discontinuity kinematics in embedded finite element method (e-fem) formulations. Materials. https://doi.org/10.3390/ma14195640

30. Ortiz M, Leroy Y, Needleman A (1987) A finite element method for localized failure analysis. Comput Methods Appl Mech Eng 61:189–214. https://doi.org/10.1016/0045-7825(87)90004-1

31. Peng Y, Chen X, Ying L, Chen Y, Zhang L (2019) Mesoscopic numerical simulation of fracture process and failure mechanism of concrete based on convex aggregate model. Adv Mater Sci Eng 2019:1–17. https://doi.org/10.1155/2019/5234327

32. Peng Y, Liu Y (2019) Advances in the Base Force Element Method. Springer, Singapore. https://doi.org/10.1007/978-981-13-5776-3

33. Raina A, Linder C (2010) Modeling crack micro-branching using finite elements with embedded strong discontinuities. PAMM 10:681–684. https://doi.org/10.1002/pamm.201010328

34. Rémond Y, Ahzi S, Baniassadi M, Garmestani H (2016) Homogenization of Reconstructed RVE. John Wiley & Sons. Ltd. chapter 6:133–168. https://doi.org/10.1002/9781119307563.ch6

35. Roubin E, Vallade A, Benkemoun N, Colliat JB (2015) Multi-scale failure of heterogeneous materials: A double kinematics enhancement for embedded finite element method. Int J Solids Struct 52:180–196

36. Salagame R, Belegundu A (1994) Distortion, degeneracy and rezoning in finite elements - a survey. Sadhana - Acad Proceed Eng Sci 19:311–335. https://doi.org/10.1007/BF02811901

37. Simo JC, Rifai MS (1990) A class of mixed assumed strain methods and the method of incompatible modes. Int J Numer Methods Eng. 29:1595–1638. https://doi.org/10.1002/nme.1620290802

38. Song JH, Wang H, Belytschko T (2008) A comparative study on finite element methods for dynamic fracture. Computat Mech 42:239–250. https://doi.org/10.1007/s00466-007-0210-x

39. Stamati O, Andò E, Roubin E, Cailletaud R, Wiebicke M, Pinzon G, Couture C, Hurley RC, Caulk R, Caillerie D, Matsushima T, Bésuelle P, Bertoni F, Arnaud T, Laborin AO, Rorato R, Sun Y, Tengattini A, Okubadejo O, Colliat JB, Saadatfar M, Garcia FE, Papazoglou C, Vego I, Brisard S, Dijkstra J, Birmpilis G (2020) 'spam': Software for practical analysis of materials. J Open Sour Soft 5:2286. https://doi.org/10.21105/joss.02286

40. Stamati O, Roubin E, Andò E, Malecot Y (2018) Phase segmentation of concrete x-ray tomographic images at meso-scale: Validation with neutron tomography. Cement and Concrete Composites 88:8–16

41. Stamati O, Roubin E, Andò E, Malecot Y (2019) Tensile failure of micro-concrete: from mechanical tests to fe meso-model with the help of x-ray tomography. Meccanica 54:707–722. https://doi.org/10.1007/s11012-018-0917-0

42. Stamati O, Roubin E, Andò E, Malecot Y, Charrier P (2021) Fracturing process of micro-concrete under uniaxial and triaxial compression: Insights from in-situ x-ray mechanical tests. Cement and Concrete Research 149:106578

43. Stanic A, Brank B, Brancherie D (2020) Fracture of quasi-brittle solids by continuum and discrete-crack damage models and embedded discontinuity formulation. Eng Fract Mech 227:106924. https://doi.org/10.1016/j.engfracmech.2020.106924

44. Strouboulis T, Copps K, Babuška I (2001) The generalized finite element method. Comput Methods Appl Mech Eng 190:4081–4193. https://doi.org/10.1016/S0045-7825(01)00188-8

45. Sukumar N, Chopp D, Moës N, Belytschko T (2001) Modeling holes and inclusions by level sets in the extended finite-element method. Comput Methods Appl Mech Eng 190:6183–6200. https://doi.org/10.1016/S0045-7825(01)00215-8

46. Sun Y, Roubin E, Shao J, Colliat JB (2021) Strong discontinuity fe analysis for heterogeneous materials: The role of crack closure mechanism. Comput Struct 251:106556. https://doi.org/10.1016/j.compstruc.2021.106556

47. Taylor RL, Govindjee S (2020) FEAP -A Finite Element Analysis Program - Version 86 Programmer Manual. Univ Calif Berk 16(20):4681–690

48. Unosson M, Olovsson L, Simonsson K (2006) Failure modelling in finite element analyses: Element erosion with crack-tip enhancement. Finite Elem Analy Des 42:283–297. https://doi.org/10.1016/j.finel.2005.07.001

49. Watwood V (1970) The finite element method for prediction of crack behavior. Nuclear Eng Desi 11:323–332. https://doi.org/10.1016/0029-5493(70)90155-X

50. Weinan E (2011) Principles of Multiscale Modeling. Cambridge University Press, Cambridge

51. Wells G, Sluys L (2001) Three-dimensional embedded discontinuity model for brittle fracture. Int J Solids Struct. 38:897–913. https://doi.org/10.1016/S0020-7683(00)00029-9

52. Zeng Q, Motamedi MH, Leong AFT, Daphalapurkar NP, Hufnagel TC, Ramesh KT (2019) Validated simulations of dynamic crack propagation in single crystals using efem and xfem. Int J Fract 215:49–65. https://doi.org/10.1007/s10704-018-0330-7

53. Zhang Y, Lackner R, Zeiml M, Mang HA (2015) Strong discontinuity embedded approach with standard sos formulation: Element formulation, energy-based crack-tracking strategy, and validations. Comput Methods Appl Mech Eng 287:335–366. https://doi.org/10.1016/j.cma.2015.02.001